Journal of Atmospheric and Solar–Terrestrial Physics 219 (2021) 105642

Contents lists available at ScienceDirect

Journal of Atmospheric and Solar–Terrestrial Physics

journal homepage: www.elsevier.com/locate/jastp

Research paper

A Na density lidar method and measurements of turbulence to 105 km at the Andes Lidar Observatory

Channing P. Philbrick [a,b,*], Fan Yang [c], Fabio A. Vargas [a], Gary R. Swenson [a], Alan Z. Liu [c]

[a] Department of Electrical and Computer Engineering, University of Illinois at Urbana–Champaign, Urbana, IL, 61801, USA
[b] Department of Electrical, Computer, & Energy Engineering, University of Colorado Boulder, Boulder, CO, 80309, USA
[c] Physical Sciences Department, Embry-Riddle Aeronautical University, Daytona Beach, FL, 32114, USA

ARTICLE INFO

Keywords:
Lidar
Atmospheric turbulence
Mesosphere & lower thermosphere (MLT) dynamics

ABSTRACT

This study presents a method of measuring atmospheric turbulence from resonance-fluorescence lidar observations of atmospheric Na layer density fluctuations, which is used to characterize turbulent eddy diffusion (k_{zz}^{Turb}) from 85 km to 105 km altitude over the Andes Lidar Observatory (ALO) in Cerro Pachón, Chile, (30.3°S, 70.7°W) at timescales between 12 seconds and 78 seconds. Na lidar measurements of heat, momentum, and constituent fluxes at turbulence scales have traditionally been limited to the 85–100 km region due to signal limitations; however, the "Na density" method described herein offers a 3x signal-to-noise ratio improvement over Doppler heat flux measurements, enabling determination of eddy diffusion to higher altitudes and at shorter timescales. The presented mean turbulent eddy diffusion profile is determined from 115 h of zenith data acquired over 25 nights via the Na density method. Results are supplemented by off-zenith data for all 25 nights, which is used to examine atmospheric stability. Mean k_{zz}^{Turb} over the timescales analyzed ranged between 1.2×10^5 cm^{2}s^{-1} and 5.7×10^5 cm^{2}s^{-1} in the 85–100 km region and increased from a minimum at 98 km to a maximum of 4.5×10^6 cm^{2}s^{-1} near 105 km altitude. The mean profile is compared with the Doppler method for (i) the same ALO dataset discussed herein and (ii) vertical-only ALO data between 85 km and 100 km altitude. The critical region (95–110 km) of diffusive coupling in the mesosphere and lower thermosphere (MLT) differs in forcing uniquely with a dominance of wind shear and associated instabilities. Source investigations pertaining to the induced transport difference from the critical to the lower MLT region (80–95 km), where the effects of damped atmospheric gravity waves and convective instabilities are well-established, require an ability to gather data on the variability of turbulence with altitude, latitude, and season, as well as atmospheric wave activity.

1. Introduction

The mesosphere and lower thermosphere (MLT) region contains the "turbopause" (~100 km altitude), which bridges the dominance of molecular diffusion above to an eddy-dominated atmosphere below (e.g. Colegrove et al., 1965, 1966; Shimazaki, 1971). The transition region of molecular versus eddy diffusion versus altitude has a major influence over the vertical distribution of minor constituents (e.g. O, H, He, CO, CO_2), as described in early studies by Allen et al. (1981, 1984) and spatiotemporal variability from observations (e.g. Shimazaki, 1971).

Turbulence and dissipating gravity waves are significant contributors to eddy diffusion in the region (e.g. Colegrove et al., 1966; Hodges, 1967; Lindzen, 1981; Gardner and Liu, 2010). In-situ sampling of atmospheric species from rocket-borne methods has been a key contributor to understanding turbulence in this region (e.g. Lübken, 1997). Measurements by the Sounding of the Atmosphere using Broadband Emission Radiometry (SABER) instrument aboard the Thermosphere Ionosphere Mesosphere Energetics and Dynamics (TIMED) satellite have been analyzed by Shuai et al. (2014) for gravity wave and tidal effects above 100 km. Swenson et al. (2019) analyzed more than a solar cycle of SABER as well as Scanning Imaging Absorption Spectrometer for Atmospheric Chartography (SCIAMACHY) data for the determination of a near-global average (between ±60° latitude) eddy diffusion (k_{zz}) profile versus altitude, a parameterization of the total eddy diffusion velocity due to turbulence and dissipating gravity waves. The Swenson et al. (2019) analysis of SCIAMACHY described k_{zz} increasing by a factor of 3x from 85 km to 105 km, with the largest values above 100 km altitude.

* Corresponding author at: Department of Electrical and Computer Engineering, University of Illinois at Urbana–Champaign, Urbana, IL, 61801, USA.
E-mail address: phlbrck2@illinois.edu (C.P. Philbrick).

https://doi.org/10.1016/j.jastp.2021.105642
Received 2 October 2020; Received in revised form 20 March 2021; Accepted 28 March 2021
Available online 8 April 2021
1364-6826/Published by Elsevier Ltd.

Turbulence is a product of atmospheric instabilities, including both convective and shear forcing. Major insights into the region above 95 km have been with chemical release experiments, which have been used to measure the winds (and shears) with altitude, at all latitudes, since 1958 (Larsen, 2002). The results include measurements of shear magnitudes that exceed 40 $ms^{-1}km^{-1}$, a shear threshold of instability, between 90 km and 115 km, with a maximum shear near 105 km. A significant contribution to the large winds and shears includes the tides, and coupling of gravity waves and tides. The shears leading to instability may be due to tides alone, but they may be enhanced when tides and gravity waves with similar vertical wavelengths cohere. The gravity waves involved are not necessarily damped or dissipating.

In summary, the global mean effective transport due to turbulence and gravity waves, derived from rocket releases of chemicals, SABER limb measurements of gravity waves, and global mean k_{zz} profiles from the climatology of atomic oxygen, is large above 100 km. More study is needed to characterize the details of the source and effects above ~100 km, especially the latitudinal, seasonal, and atmospheric wave (planetary, tides, gravity wave) variability.

The lidar methods of measuring turbulence with Na lidar have recently been achieved by Guo et al. (2017). Liu (2009) has described the method of defining k_{zz} from Doppler Na lidar measurements. The measurement capabilities of the Andes Lidar Observatory (ALO), with the power–aperture product ~0.9 Wm^2, have an upper limit of Doppler capability measurements of turbulence and heat flux of ~97 km (Gardner and Vargas, 2014; Gardner and Liu, 2014; Gardner, 2018). This study (1) describes a method, which employs a measure of atmospheric perturbations in Na density to deduce turbulence below the Brunt–Väisälä scale, extending the capability to measure k_{zz} at turbulence scales to higher altitudes than the Doppler method, and (2) describes the results of 25 nights observation of turbulence from 85 km to 105 km. The Doppler method of measuring heat flux and turbulence with Na lidar has a valued historical and resilient physical basis. The intention of presentation and utilization of the "Na density" method is to supplement and extend the altitude, where the Doppler methods have the signal-to-noise ratio (S/N) limitation, and, over time, can make a valued contribution.

2. Diffusion, gravity waves, & turbulence

2.1. Diffusion

The atmosphere is considered well-mixed and dominated by eddy diffusion below the turbopause (~100 km altitude), and molecular diffusion above. Variations in diffusion velocity and net constituent flux affect the diffusion profiles of minor species in the middle and upper atmosphere, altering atmospheric composition. While the molecular diffusion coefficients for minor species are well-known (e.g. Banks and Kockarts, 1973), the magnitude and variations of the eddy diffusion coefficient in the turbopause region are, in general, not (Swenson et al., 2018).

The total diffusion velocity, $w_i(z)$, of minor species, i, with altitude is given by Eq. (1) (Colegrove et al., 1965, 1966),

$$w_i(z) = -D_i\left[\frac{1}{[n_i]}\frac{\partial[n_i]}{\partial z} + \frac{1}{T}\frac{\partial T}{\partial z} + \frac{1}{H_i}\right] - k_{zz}\left[\frac{1}{[n_i]}\frac{\partial[n_i]}{\partial z} + \frac{1}{T}\frac{\partial T}{\partial z} + \frac{1}{H_p}\right] \quad (1)$$

where D_i is the species-specific molecular diffusion coefficient, $[n_i]$ is the minor species number density, m_i is the minor species mass, $H_i = kT/\overline{m_i}g$ is the species-specific scale height, and the pressure scale height is given by $H_p = kT/\overline{m}g$ for mean neutral mass $\overline{m} = \sum_i m_i[n_i]/\sum_i[n_i]$. Total k_{zz} is dependent on vertical fluctuations induced by tides, planetary waves, gravity waves, and turbulence, with wave-induced chemical transport enhancing or reducing total mixing (Gardner, 2018). This study examines fluctuations induced by gravity waves and turbulence only. The effect, where k_{zz} is a "parameterized" effect of turbulence and dissipating waves, describes the associated vertical constituent transport (flux) of minor species with respect to the background atmosphere.

Accordingly, the total k_{zz} in Eq. (1) may be expressed as the combination of eddy mixing contributions from both sources, as in Eq. (2).

$$k_{zz} \approx k_{zz}^{GW} + k_{zz}^{Turb} \quad (2)$$

Gravity wave- and turbulence-induced fluctuations have distinct spatial and temporal spectra, the contributions of which are separable from measurements of vertical heat fluxes and constituent densities (Gardner and Liu, 2014). It is important to note, however, that this is an approximation, as wave-induced vertical constituent flux impacts turbulence-induced eddy transport, and vice-versa (Gardner, 2018). The transport processes and determination of a near ±60° global mean k_{zz}, including the 100–105 km region, are further discussed by Swenson et al. (2019) and references therein.

2.2. Gravity waves & instabilities

Formed from tropospheric or secondary disturbances (Fritts and Alexander, 2003; Fritts et al., 2017), gravity waves transport energy and momentum upwards to the mesosphere and lower thermosphere (MLT) region through buoyancy oscillations in the local atmospheric density (Hines, 1960). Wave dissipation is a primary factor in driving the circulation structure of the MLT region (Fritts and Vanzandt, 1993). Turbulence and gravity wave dissipation are also important considerations of upper atmospheric composition modelings (e.g. Colegrove et al., 1965; Shimazaki and Whitten, 1976; Marsh and Garcia, 2007; Qian et al., 2009; Marsh et al., 2013).

Turbulence results from unstable atmospheric conditions which causes vertical mixing. The Brunt–Väisälä frequency, N, is the parameter relevant to stability (Gossard and Hooke, 1975),

$$N^2 = \frac{g}{T}\left(\Gamma_{ad} + \frac{\partial T}{\partial z}\right) \quad (3)$$

where g is gravitational acceleration, $\partial T/\partial z$ is the atmospheric lapse rate, and Γ_{ad} is the adiabatic lapse rate (~9.5 K/km). Convective instability, which leads to vertical mixing, occurs when $N^2 < 0$, even with the absence of vertical wind shear. Kelvin–Helmholtz instabilities (KHI, associated with vertical wind shear) are characterized by the Richardson number, Ri, which is defined as the ratio of N^2 to the square of the vertical shear of the horizontal wind (Richardson, 1920).

$$Ri = \frac{N^2}{(\partial U/\partial z)^2} \quad (4)$$

$$\left(\frac{\partial U}{\partial z}\right)^2 = \left(\frac{\partial u}{\partial z}\right)^2 + \left(\frac{\partial v}{\partial z}\right)^2 \quad (5)$$

In Eq. (5), wind shear, $\partial U/\partial z$, is specified in terms of its zonal $(\partial u/\partial z)$ and meridional $(\partial v/\partial z)$ components. KHI occur where the necessary condition $Ri < 1/4$ is satisfied (Hines, 1971; Gossard and Hooke, 1975). Given a nominal lapse rate ($N^2 = 10^{-4}$ s^{-2}), a wind shear in excess of 40 $ms^{-1}km^{-1}$ in the MLT region is the threshold of shear instability ($Ri \sim 1/4$) which normally leads to turbulence and vertical mixing.

Chapter 6 of Nappo (2012) describes the theoretical rationale of stability criteria and the stable conditions for $Ri > 1/4$, and flow instability having a necessary condition of $Ri < 1/4$. The KHI process involves layer mixing at the shear boundary where the less dense layer elements are buoyant leading to convective instabilities, and subsequently breaking down into turbulence (Nappo, 2012). In this case, a dynamic instability leads to a convective instability and turbulence. Dynamical instabilities can further lead to secondary convective instabilities (Palmer et al., 1996). Stable stratified shear flows have been studied by Miles and Howard (1964), wherein $Ri < 1/4$ are stable. In this case, there is little mixing between the adjacent shear layer densities, and consequently, less dense parcels do not mix, and convective

instabilities do not develop. The $Ri < 0$ limit is the convective limit ($N^2 < 0$). Note that Eqs. (3) and (4) are coupled: where the temperature lapse rate in the mesopause is negative (low N^2), vertical shears less than 40 $ms^{-1}km^{-1}$ will result in $Ri < 1/4$ (unstable conditions).

The past 20 years have provided new insights into the physical processes involved with breaking waves and their effects on the MLT. Simulations of breaking gravity waves and turbulence have been studied in detail (e.g. Fritts and Alexander, 2003; Fritts et al., 2017, 2018). Technologies including computational power enable complex, detailed simulation studies. Technology evolution of Doppler lidar, imagers, and radar are providing new insights and understanding of gravity wave damping leading to turbulence in the MLT. In the MLT, gravity waves with sufficient energy can disrupt a critically-stable atmosphere through wave–tide and wave–wave interactions (e.g. Hodges, 1967; Hecht, 2004; Li et al., 2005a,b; Yue et al., 2010; Guo et al., 2017), creating one or more instability regions. Ripples in the airglows originating in the MLT (80–105 km) altitude region are manifestations of instabilities, whose distinct patterns appear along (parallel to) phase fronts, indicative of convective instabilities, and billow structure orthogonal to the phase fronts, indicative of shear instabilities (Hecht, 2004). These features are statistically prevalent in the MLT regions (Hecht, 2004). One example of vertical shears from waves in the MLT at latitudes equatorward of 30° is the diurnal tide, where amplitudes exceed 100 ms^{-1} between phases ($\partial z \sim 10$ km), resulting in a shear of $\sim 20\ ms^{-1}km^{-1}$. Under conditions of low N^2, a large tidal induced shear alone is sufficient to result in a potentially unstable atmosphere (Li et al., 2009).

Subsequently, evolution of the instability regions leads to net vertical constituent transport as a result of atmospheric turbulence (e.g. Hodges, 1969; Lindzen, 1981; Zhao et al., 2003). Displacement of atmospheric parcels give rise to fluctuations in temperature and horizontal and vertical wind profiles at frequencies lower (higher) than N for gravity waves (turbulence). An important finding by Gardner (2018) using Na Doppler lidar observations from both Starfire Optical Range, NM (SOR, 35°N, 106.5°W) and the Andes Lidar Observatory, Chile (ALO, 30.3°S, 70.7°W), the vertical heat and constituent fluxes from breaking gravity waves far exceeds turbulence from instabilities by a factor of ~3. Fritts et al. (2018) has similar findings below 95 km in the simulations and study of mesospheric inversion layers (MILs).

For further insight into the role of gravity waves on turbulence and transport, see Hines (1960), Fritts and Alexander (2003), Nappo (2012), Fritts et al. (2017), and Gardner (2018).

2.3. Atmospheric turbulence

Atmospheric turbulence in the MLT region is predominantly generated from interactions between planetary waves, tides, and gravity waves. Fluctuations resulting from organized (chaotic) motions due to waves (turbulence) are present in temperature, wind, and density profiles. The spatial and temporal spectra of turbulent motions have been found observationally (e.g. Thrane and Grandal, 1981; Lübken, 1997; Guo et al., 2017) to follow the theoretical power law first proposed by Kolmogorov (1941) and later refined in the turbulence spectral model of Heisenberg (1948).

The inertial subrange of the turbulence vertical wavenumber spectrum is given by Eq. (6) (Weinstock, 1981; Lübken, 1997),

$$S(m) = \alpha \epsilon^{\frac{2}{3}} m^{-\frac{5}{3}} \tag{6}$$

for Kolmogorov constant α, turbulent energy dissipation rate ϵ, and vertical wavenumber m. The inertial subrange is bounded by the outer scale l_o and inner scale l_i, with $(m_o = 2\pi/l_o) \leq m \leq (m_i = 2\pi/l_i)$ and (Weinstock, 1978, 1981; Lübken, 1997; Gardner and Liu, 2014)

$$\begin{aligned} l_o &= 9.97\sqrt{\frac{\epsilon}{N^3}} \\ l_i &= 9.90\left(\frac{\nu^3}{\epsilon}\right)^{\frac{1}{4}} = 9.90\eta \end{aligned} \tag{7}$$

Here, ν is the kinematic viscosity and η is the Kolmogorov microscale. MLT observations suggest that an outer scale of $l_o \approx$ 100–3000 m and inner scale of $l_i \approx$ 10–30 m are typical (Lübken, 1997; Das et al., 2009).

The turbulent eddy diffusion coefficient, k_{zz}^{Turb}, is connected to the turbulent energy dissipation rate by Eq. (8) (Weinstock, 1978, 1981)

$$k_{zz}^{Turb} = \frac{\alpha^{\frac{3}{2}}\sqrt{\pi}}{4}\left(\frac{\epsilon}{N^2}\right) \tag{8}$$

such that the total spectral power over the inertial subrange can be related to k_{zz}^{Turb} by Eq. (9).

$$k_{zz}^{Turb} = \frac{\sqrt{\pi}}{4N^2}\left[\frac{P_{Turb}}{\frac{3}{2}\left(m_o^{-\frac{2}{3}} - m_i^{-\frac{2}{3}}\right)}\right]^{\frac{3}{2}} \tag{9}$$

The turbulent energy dissipation rate is determined by integrating Eq. (6) over the bounds in Eq. (7). The resulting expression is then combined with Eq. (8) to yield Eq. (9). The total turbulence spectral power, P_{Turb}, is defined as $P_{Turb} = \int_{m_o}^{m_i} S(m)dm$. This expression is subject to the limitations of the approximations discussed by Weinstock (1978) and Lübken (1997).

In the viscous dissipation range ($m > m_i$), the vertical wavenumber spectrum is proportional to m^{-7}, while for $m < m_o$, the spectrum is controlled by source characteristics (Gardner and Liu, 2014). The temporal turbulence spectrum follows the same power laws under Taylor's frozen-in hypothesis (Taylor, 1935), which states that turbulent eddies are advected horizontally by the mean wind. The temporal outer and inner scales, therefore, are related to the spatial scales by $\omega_o = \bar{u}m_o$ and $\omega_i = \bar{u}m_i$, respectively (Gardner and Liu, 2014), where $\bar{u}$ is the mean horizontal wind.

For the inertial and viscous dissipation subranges, the applicable power laws imply that the largest eddies contain the greatest energy. This trait is useful in scenarios where, due to S/N and/or resolution limitations, the full turbulence wavenumber spectrum cannot be measured. Discarding the high-frequency components of the spectrum increases measurement uncertainty but still permits collection of scientifically valuable data. It is important to note that the slope of the observed turbulence spectra may show a depletion at small scales due to diffusion.

The gravity wave vertical wavenumber spectrum is also both theorized and observed to follow a power law (Gardner, 1996). The temporal gravity wave spectrum is bounded by the inertial frequency and N (Hines, 1960), between which the spectrum is proportional to ω^{-2}. The vertical wavenumber spectrum follows an m^{-3} power law (Gardner and Yang, 1998; Gardner, 1998). In the mesopause region, vertical wavelengths range from around 100 km to 1 km, with $N/2\pi \approx 3$ mHz (Liu, 2009; Gardner and Liu, 2010; Guo et al., 2017). Based on the gravity wave and turbulence inertial subrange cutoffs, the contributions of each may be roughly separated by filtering below and above the transition frequency. The turbulence and viscous subranges can also be similarly differentiated.

3. Na resonance-fluorescence lidar

Atmospheric turbulence has been measured experimentally through several approaches (e.g. Rees et al., 1972; Thrane and Grandal, 1981; Sato et al., 1985; Widdel, 1985; Schmidlin et al., 1991; Meriwether et al., 1994; Lübken, 1997; Bishop et al., 2004), with first parameterization of eddy diffusion transport due to turbulence (k_{zz}^{Turb}) made by Colegrove et al. (1966). Recently, Na resonance-fluorescence lidar systems, such as that at the Andes Lidar Observatory (ALO), have achieved sufficiently large power–aperture products to measure atmospheric turbulence in the MLT region (Bills et al., 1991; Liu et al., 2016; Guo et al., 2017). Three-frequency resonance-fluorescence lidar systems can simultaneously measure temperature, line-of-sight wind

speeds, and Na density (TWD) at high resolution (Krueger et al., 2015). The ALO system, for example, has achieved a vertical resolution of 25 meters and temporal resolution of six seconds.

The resonance-fluorescence technique is reliant on the presence of trace metallic species (Na, K, Li, Ca, and Fe) layers in the vertical region of interest. Such layers are formed from meteoric ablation and cosmic dust and are found between 70 km and 120 km altitude (Plane, 1991). The Na layer typically has a peak density of several thousand cubic centimeters near 92.5 km altitude and a full-width half-maximum (FWHM) of 10 km (Gardner et al., 2017).

Measurements are taken at three frequencies, with temperature, wind, and Na density profiles reconstructed either through iterative (e.g. Papen et al., 1995; Chu and Papen, 2005; Krueger et al., 2015) or inversion (e.g. Gardner and Liu, 2014; Gardner and Vargas, 2014; Guo et al., 2017) techniques. In the MLT region, temperature, vertical wind, and horizontal wind uncertainties of ±5 K, ±1 m/s, and ±3 m/s, respectively, are typical at 80 s, 500 m resolution for a Na lidar system with a power–aperture product of 0.9 Wm^2. The Na lidar S/N is defined in Eq. (10) (Liu et al., 2016),

$$S/N = \frac{C_S}{\sqrt{C_S + C_B}} \tag{10}$$

where C_S and C_B are respectively signal and background photocounts. Further detail on the resonance-fluorescence lidar technique is readily available in the literature (e.g. Chu and Papen, 2005).

3.1. Challenges of the doppler method

Past resonance-fluorescence lidar measurements of eddy diffusion have employed the "Doppler" method, for which the eddy diffusion coefficient is determined with altitude from measurements of heat flux ($\overline{w'T'}$) via Eq. (11) (Gardner and Yang, 1998; Liu, 2009; Gardner and Liu, 2014; Guo et al., 2017),

$$\overline{w'T'} \approx -k_H \left(\Gamma_{ad} + \frac{\partial \overline{T}}{\partial z} \right) \tag{11}$$

where $\overline{\zeta}$ denotes the average parameter profile taken at a resolution lower than the longest period of the feature of interest, $\zeta' = \zeta - \overline{\zeta}$ denotes detrended perturbations about $\overline{\zeta}$, w is the vertical wind speed, and the thermal diffusion coefficient $k_H \approx k_{zz}$. Contributions of gravity waves and turbulence to temperature and vertical wind perturbations are spectrally separable (Gardner and Liu, 2014), thereby permitting measurement of both k_{zz}^{Turb} and k_{zz}^{GW} from heat flux measurements.

The current power–aperture product of the ALO Na resonance-fluorescence lidar permits estimation of k_{zz}^{Turb} within approximately ±10 m^2/s in the 85–97 km region under the Doppler method (Guo et al., 2017). Above 97 km, wind and temperature errors become significant, even at long integration times, due to decreasing Na layer density. To measure k_{zz}^{Turb} within ±10 m^2/s, turbulence-induced fluctuations in the vertical wind and temperature profiles must be measured within ±1 m/s and ±1 K, respectively (Guo et al., 2017). At MLT heights, this corresponds to a temperature measurement precision of ±0.3% (S/N of ~333 in shot noise-limited systems with negligible background) (Papen et al., 1995).

In contrast, a measurement method relying solely on Na layer density fluctuations, such as that discussed herein, requires determination of detrended Na number density fluctuations ($[Na]'/\overline{[Na]}$) to within ±1% (S/N of ~100) to achieve the same k_{zz}^{Turb} measurement uncertainty (Lübken, 1997). In other words, given the mean photocount profile presented in this study, the S/N for a $\overline{w'T'}$ measurement uncertainty of ±10 m^2/s at 97 km occurs at 105 km for the density-only approach. Therefore, by implementing the approach of this study, which does not require the higher S/N measurements of w' or T', it is possible to extend the maximum measurement altitude of turbulence parameters without compromising resolution.

3.2. Na perturbations

The Na layer acts as a passive, chemically inert tracer of gravity wave and turbulent motion in the 85–105 km region (Hickey and Plane, 1995). Scale height differences between the Na layer and the background atmosphere result in variable layer sensitivity. At peak Na layer density gradients, $[Na]$ perturbations can reach amplitudes of 10–15 times those of neutral fluctuations (Kelley et al., 2003; Gardner and Liu, 2014). Measurements of turbulence-induced neutral density fluctuations, in contrast, are unbiased with altitude and thus suitable for determining vertical k_{zz}^{Turb} profiles. Na and neutral perturbations are related by Eq. (12) (Thrane and Grandal, 1981; Kelley et al., 2003),

$$\frac{[N]'}{\overline{[N]}} = \left(\frac{\gamma H_p/H_n - 1}{\gamma H_p/H_{Na} - 1} \right) \frac{[Na]'}{\overline{[Na]}} = F \frac{[Na]'}{\overline{[Na]}} \tag{12}$$

where $\gamma \approx 1.45$ (Lübken, 1997), $[N] \approx [N_2] + [O_2]$ is the neutral/background number density, and the neutral and Na "scale heights", denoted H_n and H_{Na}, respectively, are given by Eqs. (13)–(14).

$$\frac{1}{H_n} = \frac{1}{H_p} + \frac{1}{\overline{T}} \frac{\partial \overline{T}}{\partial z} \tag{13}$$

$$\frac{1}{H_{Na}} = -\frac{1}{\overline{[Na]}} \frac{\partial \overline{[Na]}}{\partial z} \tag{14}$$

As in the case of Eq. (11), $\overline{\zeta}$ is the average profile and ζ' are the detrended perturbations with respect to $\overline{\zeta}$. The vertical wavenumber spectrum, $S(m)$, is determined from the neutral density fluctuation spectrum for zenith measurements.

The Na density approach requires vertical measurements of Na layer perturbations at high resolution and background temperature and Na density at low resolution. While measurement uncertainty can be reduced for $\overline{T}$ and $\overline{[Na]}$ by binning profiles prior to reconstruction, it cannot for Na layer perturbations due to resolution requirements. Accordingly, measurement uncertainty is limited by uncertainty in the estimated $[Na]'/\overline{[Na]}$ profile. Given that the Na density and photocount fluctuation profiles are approximately equal (the validity of this relation is discussed in Section 4), measurement uncertainty is driven by mean signal returns in the shot noise-limited case. Specifically, a 1% uncertainty in $C'/\overline{C}$ corresponds to a 1% uncertainty in $[Na]'/\overline{[Na]}$. Thus, the S/N improvement over the Doppler method discussed in Section 3.1 is realized.

The remainder of this study examines resonance-fluorescence lidar measurements of Na layer density fluctuations at turbulence scales, relating layer perturbations to k_{zz}^{Turb} through Eq. (9), Eq. (12), and the methodology described herein. Average turbulent eddy diffusion profiles, determined from 25 nights of lidar data between 85 km and 105 km altitude, are compared against Doppler method observations and found to agree favorably.

4. Data processing

The Na density method determines time-average k_{zz}^{Turb} with altitude from Na resonance-fluorescence lidar measurements. First, the Na layer perturbation profile, $[Na]'/\overline{[Na]}$, is calculated and filtered in both the spatial and temporal domains to retain fluctuations at turbulence scales only. In this study, $[Na]'/\overline{[Na]}$ measurements were temporally averaged to determine mean nightly vertical perturbation profiles. The neutral density perturbation profile, $[N]'/\overline{[N]}$, is next calculated from $[Na]'/\overline{[Na]}$ via Eq. (12). In Eq. (12), mean temperature and Na density profiles were determined using the three-frequency TWD method. Lastly, the turbulent eddy diffusion coefficient is determined from total integrated neutral density fluctuation spectral power via Eq. (9). Background temperature and Na density profiles are obtained by binning and smoothing the high-resolution TWD profiles.

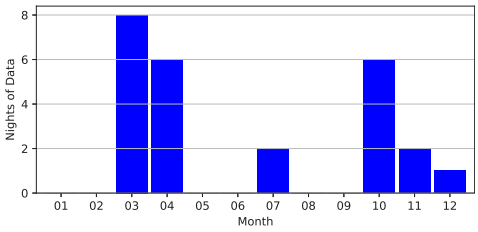

Fig. 1. Twenty-five (25) nights of temperature, vertical and horizontal wind, and Na density measurements were acquired using the ALO Na resonance-fluorescence lidar for a total of 230 h of data at 25 m, 6 s resolution. Measurements are biased towards the equinoctial periods.

4.1. Data collection

Measurements in this study were determined from 25 nights of observational data acquired between 85 km and 105 km altitude using the three-frequency Na resonance-fluorescence lidar at ALO, totaling 230 h (115 h each) of zenith and off-zenith data. The central laser frequency is locked to the D_{2a} line, with positive and negative frequencies spaced ±630 MHz from the central frequency (Liu et al., 2016). At ALO, line-of-sight wind, temperature, and Na density are measured in three directions: zenith, 20° off-zenith to the south, and 20° off-zenith to the east. For nights where off-zenith data is collected, the lidar is operated in a repeated zenith-south–zenith-east (ZSZE) sequence. Due to S/N limitations, observations at ALO are only possible at night from approximately 2300 UT to 0900 UT.

The monthly distribution of measurements used in this study is shown in Fig. 1. Off-zenith observations were collected for all nights. During the ZSZE sequence, data was acquired at 25 m, 6 s resolution for a continuous 78-second period in each direction. The continuous integration time places a bound on the largest turbulence scales that can be measured. While only zenith observations are required for measurement of k_{zz}^{Turb} by the Na density method (assuming that vertical winds are small, i.e. $|w| \leq 3$ ms^{-1} Krueger et al., 2015), measurement periods that included off-zenith observations were chosen for the current study to permit comparison of k_{zz}^{Turb} and Ri with altitude. Only zenith observations were used in calculation of k_{zz}^{Turb}. For measurements involving comparison of zenith and off-zenith observations, such as temperature and horizontal wind for calculation of Ri, off-zenith data was interpolated in altitude to the zenith profile.

Photocount profiles were corrected for photometer saturation, background contributions, $1/R^2$ falloff, and laser power fluctuations. Nonlinear photometer behavior due to saturation was corrected by Eq. (15) (Hakamata, 2007),

$$C(z,t) = \tilde{C}(z,t)\left[1 - t_{pp}\frac{f_s}{n_c}\tilde{C}(z,t)\right]^{-1} \tag{15}$$

where $\tilde{C}(z,t)$ is the uncorrected photocount profile (at 25 m, 6 s resolution), $f_s = 6$ MHz is the range gate, $n_c = 8192$ is the number of vertical integration bins, and $t_{pp} = 70$ ns is the pulse pair resolution. Error due to uncertainty in Eq. (15) was found to be minimal for the dataset analyzed due to good count linearity in the 85–105 km region (Liu and Guo, 2016). Background noise was estimated from mean returns between 125 km and 140 km altitude for each vertical profile, then subtracted from each integration bin. Na layer saturation is negligible for the ALO resonance-fluorescence lidar; therefore, correction for layer saturation is not required (Papen et al., 1995; Chu and Papen, 2005).

Laser power fluctuations were corrected using atmospheric (Rayleigh) backscatter returns between 22.5 km and 32.5 km altitude. Each six-second vertical profile was fit via linear least-squares to the theoretical Rayleigh backscatter profile given by Eq. (16) (Bills et al., 1991),

$$r(z;t) = \ln\left\{C(z;t)\left(\frac{z}{z_R}\right)^2\right\} \tag{16}$$

where $C(z;t)$ is the vertical photocount profile for a given six-second time slice t. Rayleigh returns were estimated from the fit at a reference altitude (z_R) of 27.5 km. Each six-second vertical photocount profile at Na layer altitudes (85–105 km) was then normalized by the corresponding Rayleigh reference, accounting for temporal variations in mean photocount returns.

4.2. Background parameters

Background temperature, vertical and horizontal wind, and Na density profiles used in the calculation of N^2 (Eq. (3)), Ri (Eq. (4)), H_n (Eq. (13)), and H_{Na} (Eq. (14)) were determined using the iterative TWD method. Vertical (horizontal) photocount profiles were binned to 250 m, 160 s (320 s) resolution prior to reconstruction. After reconstruction, the TWD profiles were smoothed with a 500-m, 15-min FWHM Hamming window. Brunt–Väisälä frequency (N) and scaling factor (F) profiles respectively used in the calculation of Eq. (9) and (12) were further temporally averaged to produce nightly vertically-resolved profiles at 250 m resolution (and low-pass filtered at 500 m). Nightly background parameter variances are included in the error terms for the Na layer perturbation, neutral density perturbation, and k_{zz}^{Turb} profiles presented in this study.

4.3. Na layer perturbations

Na layer perturbations ($[Na]'/\overline{[Na]}$) were determined from corrected photocounts binned to 25 m, 12 s resolution. After applying the corrective procedures described in Section 4.1, the detrended photocount fluctuation profile, $C'/\overline{C}$, is approximately equal to $[Na]'/\overline{[Na]}$, with the exception of photocount variations in the perturbed profile (with respect to the mean profile, $\overline{C}$), C', due to variations of the Na resonance-fluorescence cross-section arising from small-scale perturbations of temperature and vertical wind (cf. Eq. 5.44 and associated discussion in Chu and Papen, 2005). To reduce the impact of cross-section variations, corrected photocounts at the three observation frequencies were averaged, with profile weightings given by the background temperature ratio, R_T, used in the three-frequency method (Chu and Papen, 2005).

$$R_T = \frac{C_+ + C_-}{C_0} \tag{17}$$

In Eq. (17), subscripts correspond to the corrected photocount profiles at either the negative (C_-), positive (C_+), or central (C_0) measurement frequencies. Via this method, Na layer perturbation uncertainty due to cross-section variations over the span of $\overline{[Na]}$ was found to be small (<0.8%) as compared to layer perturbations (4%–20%). Worst-case perturbation uncertainty due to cross-section variations is included in the presented error terms.

Individual 78 s weighted photocount profiles were separately processed in the calculation of $\overline{C}$. The weighted profiles were first temporally averaged, resulting in a single 25 m resolution vertical profile for each 78 s collection period. Mean vertical profiles were then low-pass filtered with a 500 m FWHM one-dimensional Hamming window to minimize the impact of features with spatial frequencies greater than m_o (Gardner and Liu, 2010). Weighted photocount profiles were detrended via Eq. (18),

$$\frac{[Na]'}{\overline{[Na]}} \approx \frac{C'}{\overline{C}} = \frac{C - \overline{C}}{\overline{C}} \tag{18}$$

yielding Na perturbation profiles at 25 m, 12 s resolution for each 78 s collection period. Note that for continuous vertical observation periods, a 500 m, 150 s FWHM Hamming window should instead be used for detrending (Guo et al., 2017).

The Na perturbation profiles were next spatially high-pass filtered to isolate fluctuations in the turbulence subrange. A Hamming filter topology was used, with a stopband frequency of 0.8 km^{-1}, passband

frequency of 1.2 km^{-1}, and cutoff frequency of $m_o/2\pi$ = 1.0 km^{-1}. The selected parameters correspond to a peak approximation error of −43 dB, such that stopband leakage and passband ripple were minimal. Including the impact of the turbulence spectrum, the 0.8–1.0 km^{-1} band has 6% total transmission, while the 1.0–1.2 km^{-1} band has 43% total transmission. This results in a 2% loss across the bandpass region (1–20 km^{-1}). Transition band leakage, while non-negligible, is permissible, as the selected cutoff frequency is not a discrete cutoff of turbulence (Gardner and Liu, 2014).

The temporal spectra of the filtered Na perturbation profiles were fit to Eq. (6) via non-linear least squares. As with detrending, each 78 s profile was treated independently. The measurable temporal spectrum is defined by the continuous observation time of the lidar measurements (78 s) and resolution of the data (12 s), respectively corresponding to $\omega_{min}/2\pi$ = 13 mHz and $\omega_i/2\pi$ = 40 mHz. Measurement error variance was estimated from Eq. (19) (Gardner and Liu, 2014),

$$\mathrm{Var}\,[\Delta C] = \frac{1}{\Delta t \Delta z} S_{[Na]'/\overline{[Na]}}(\omega, m) \tag{19}$$

where ΔC is the photocount measurement error, $S_{[Na]'/\overline{[Na]}}(\omega, m)$ is the filtered spatiotemporal Na layer perturbation spectrum, and Δz and Δt are the spatial and temporal resolution, respectively. Statistical error variances for turbulence and noise power spectra were given by the least-squares parameter covariance matrix.

Total Na layer perturbation spectral power in the observable turbulence subrange is given by Eq. (20),

$$P_{[Na]'/\overline{[Na]}}(z) = \frac{1}{\pi}\int_{\omega_{min}}^{\omega_i} S_{[Na]'/\overline{[Na]}}(\omega; z)\partial\omega \tag{20}$$

where $S_{[Na]'/\overline{[Na]}}(\omega; z)$ is the Na layer perturbation power spectral density at altitude z. For each night of data, the spatiotemporal spectra from continuous observation periods were combined into a mean altitude-resolved spectral profile. The least-squares fit and Eq. (20) were then applied to each altitude slice independently. After integration, the nightly spectral power profiles were binned to 250 m vertical resolution. Since the background parameters are slowly-varying with respect to the integration bounds, neutral density perturbation spectral power, $P_{[N]'/\overline{[N]}}$, is related to $P_{[Na]'/\overline{[Na]}}$ via Eq. (21).

$$P_{Turb} = P_{[N]'/\overline{[N]}} = F^2 P_{[Na]'/\overline{[Na]}} \tag{21}$$

P_{Turb} and F are defined as in Eqs. (9) and (12), respectively. From Eq. (21), k_{zz}^{Turb} is determined via the relation in Eq. (9). The nightly mean $P_{[N]'/\overline{[N]}}$, $P_{[Na]'/\overline{[Na]}}$, and k_{zz}^{Turb} profiles presented in this study were determined at 250 m resolution.

For $\omega_{min}/2\pi$ = 13 mHz and assuming a nominal Brunt–Väisälä frequency of 3 mHz, a considerable portion of the turbulence subrange was not observed in the acquired data. Accordingly, the total k_{zz}^{Turb} was likely larger than that presently reported for both the Doppler and Na density methods. With a maximum spatial resolution of 20 km^{-1}, the inner scale of turbulence, $m_i/2\pi \approx 30$ km^{-1}, was also absent from the measured spectrum. Therefore, the maximum spatial resolution is an approximation to the anticipated inner scale. Since the largest scales of turbulence contain the greatest energy ($S(m) \propto m^{-5/3}$), the impact of this approximation on the total spectral power, P_{Turb}, is negligible.

4.4. Temporal resolution

While signal returns in the 102–105 km region averaged 40 counts/bin at 25 m, 12 s resolution, returns above 105 km altitude were on average too small (<25 counts/bin) for accurate reconstruction (Hayya et al., 1975), as seen in Fig. 2a. For a shot noise-limited system with negligible background (S/N $\approx \sqrt{C}$), the average S/N of 4.5 at 105 km requires a 100-minute observation period to reach an S/N of 100, which is necessary for measurement of Na layer perturbations within ±1%. Therefore, intra-nightly characterization of turbulence is possible, albeit at a low resolution for an average 8–10 hour data collection period at ALO. The integration time is perhaps better suited to determining monthly, seasonal, and annual trends from multiple nights of measurement. Annual results are presented in this study for the purpose of comparison against independent measurements of k_{zz}^{Turb} from multiple methods.

5. Mean background & stability characteristics

Average Na density, temperature, and vertical wind profiles over the 25 nights of ALO data analyzed are shown in Fig. 2b–d, respectively. Profiles were first binned from 25 m, 6 s resolution to 500 m, 160 s resolution to improve signal, then smoothed with a 1 km, 30 min Hamming window to reduce the impact of small-scale variability in the data. The measured Na density profile closely matched the anticipated theoretical layer distribution, which is Gaussian with a peak density of 4000 cm^{-3} at 92.5 km and a FWHM of 10 km (Gardner et al., 2017). Density variations were considerable, with a standard deviation larger than 2000 cm^{-3} – or half the peak layer density – at 93 km. Observed layer variability is primarily attributed to wave activity, sporadic Na layers (e.g. Qian et al., 1998), and seasonal variations in peak density. The 25-night mean profiles presented in Fig. 2 are for informative purposes only and were not used in calculation of Eq. (12).

The altitude-resolved mean temperature profile was determined from 85 km to 107 km, with a maximum per-bin uncertainty of ±10 K. At an altitude of 105 km, the average temperature reconstruction error per 500 m, 160 s bin was ±5 K. The "double mesopause" feature, with local minima at 85 km and 102 km, is commonly observed in the MLT region (e.g. She et al., 1993). The negative temperature gradient between 95 km and 102 km associated with the double mesopause aids in convective destabilization of the local atmosphere. Vertical wind measurements were limited to a maximum altitude of 100 km due to low signal returns.

Fig. 3a–c respectively show parameter likelihood with altitude for N^2, wind shear, and Ri over the 25-night dataset. Parameter distributions were each determined at 500 m, 160 s resolution using the smoothed TWD profiles and normalized to unity over the 85–105 km region. Note that in the calculation of Ri (Eq. (4)), horizontal wind profiles (determined using off-zenith measurements) were interpolated in altitude to the zenith sampling grid. Fig. 3d shows the likelihood with altitude (at 500 m resolution) that the conditions necessary for convective and KH instabilities to occur ($Ri < 0$ and $0 \leq Ri < 1/4$, respectively) are satisfied. Ri is a strong indicator of instabilities, and is informative (Li et al., 2005a). Stability data is included as a supplement and is not critical to measurement of turbulence by the Na density method.

As seen in Fig. 3a, N^2 was on average 5×10^{-4} s^{-2} in the 85–105 km region, reaching a minimum at 97.5 km. N^2 (and expected convective stability) increased above the turbopause, largely due to the positive temperature gradient. Mean wind shear magnitude, shown in Fig. 3b, was 25 ms^{-1}km^{-1} over the region examined, with a standard deviation of 15 ms^{-1}km^{-1}. This suggests that periods of high wind shear (magnitude on the order of 40 ms^{-1}km^{-1}) were somewhat infrequent throughout the observation period. The nominal dynamic stability threshold, calculated from the mean N^2 profile (with altitude) and Ri = 0.25, is also shown in Fig. 3b. Regions of high wind shear, associated with KHIs, were most common between 92 km and 102 km altitude. The Ri distribution is shown in Fig. 3c. Average Ri was smallest in the 92–102 km region, ostensibly due to the impact of mesospheric inversion layers (MILs) on MLT dynamics (e.g. She et al., 1993; Meriwether et al., 1994; Huang et al., 1998; Liu and Hagan, 1998; Meriwether and Gardner, 2000; Huang et al., 2002; Li et al., 2005a). Mean Ri between 85 km and 105 km altitude was 0.88, indicating a stable atmosphere in the average case, as expected. This agrees well with the results of Zhao et al. (2003), who found average Ri in the MLT region to range between 0.68 and 1.06 annually.

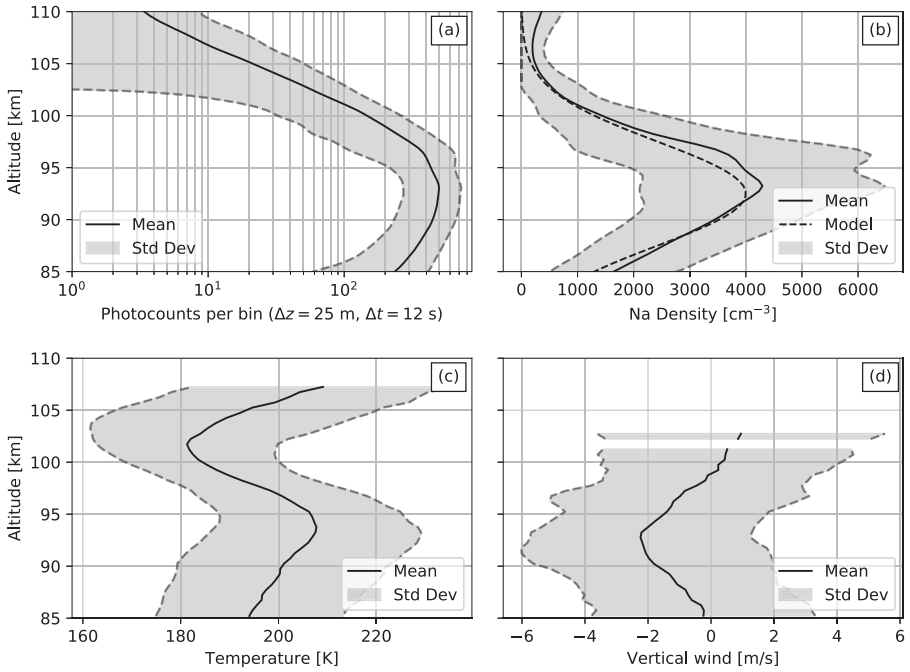

Fig. 2. (a) Average photocount return per 25 m, 12 *s* spatiotemporal bin as determined from 25 nights of observational lidar data at ALO. Profile standard deviation is denoted by the bounded shaded region. Data was collected from 85 km to 110 km, but only results in the 85–105 km region were considered due to S/N limitations. (b) Mean Na density. The theoretical annual mean Na layer profile, represented by the dashed line, is also included. While the mean profile closely matched the theoretical curve, Na layer density varied considerably. Density reconstruction error is less than 1 cm^{-3} in the 85–105 km region and as such is not shown. (c) Mean temperature profile. Nightly measurements with uncertainty in excess of 25 K were omitted from the shown statistics. (d) Mean vertical wind profile. Measurements with uncertainties greater than 5 ms^{-1} are discarded, with the effective measurement range limited to 85–100 km altitude due to poor signal returns.

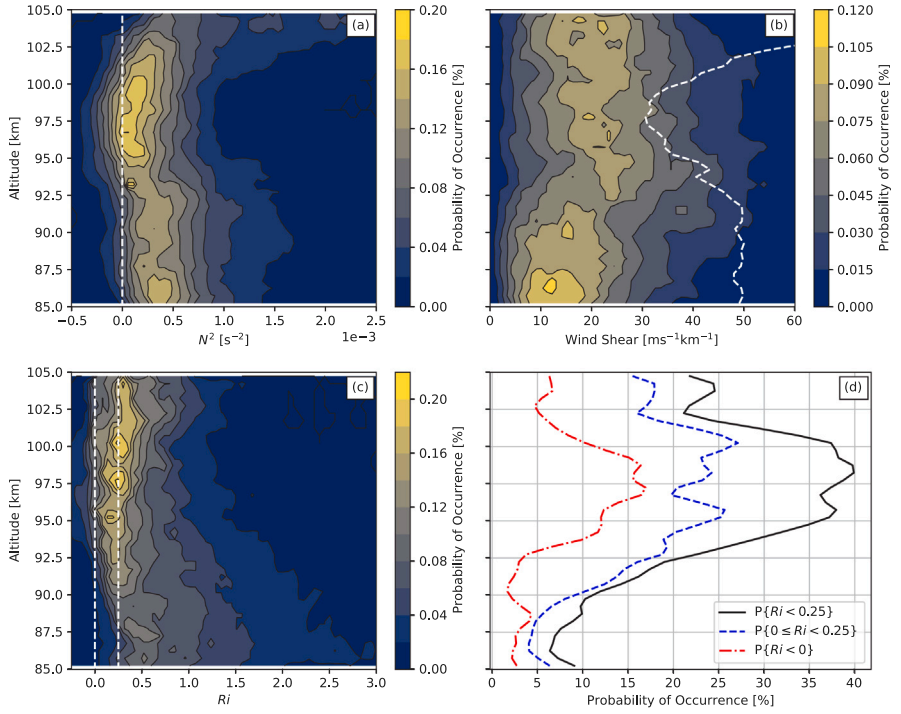

Fig. 3. (a) Square Brunt–Väisälä frequency (N^2) probability distribution with altitude, as determined from 25 nights of lidar data acquired at ALO. The distribution is normalized across the 85–105 km region. The critical threshold of static stability, $N^2 = 0$, is marked for clarity. (b) Mean vertical shear of the horizontal wind with the nominal dynamic stability (KHI) threshold co-plotted (dashed). (c) Mean Richardson number (Ri) profile. The traditional stability thresholds ($Ri = 0$ and $Ri = 1/4$) are denoted by vertical dashed lines. (d) Average instability threshold probability distribution.

The likelihoods of $Ri < 0$, $0 \leq Ri < 1/4$, and $Ri < 1/4$ are shown in Fig. 3d. Likelihood increased (decreased) sharply near 90 km (102 km) altitude, with a maximum combined likelihood near 40% at 98 km. At 85 km and 105 km, the total likelihood fell to 25%. Across the region examined, the average probability that either the convective or dynamical thresholds were met at any one time was 23%. At all altitudes, the dynamical instability threshold was observed to occur more frequently than that of convective instability. Below 92 km,

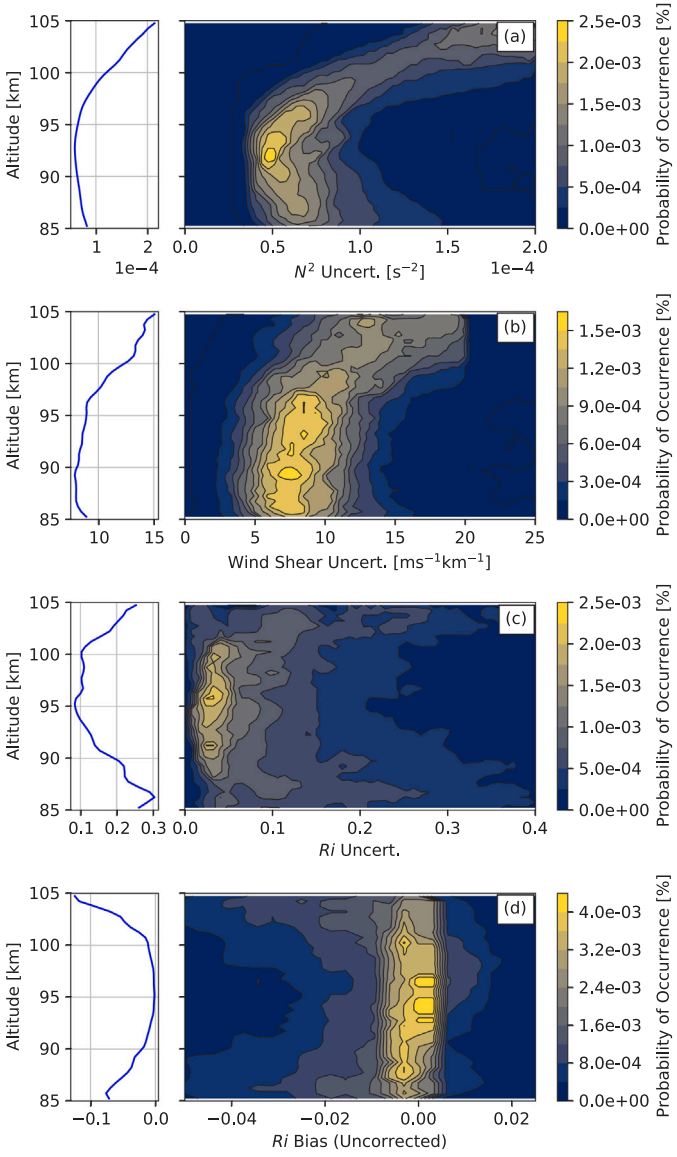

Fig. 4. (a)–(c) N^2, wind shear, and Ri uncertainty distributions with altitude, respectively. (d) Estimated uncorrected Ri measurement bias distribution with altitude. Profiles are normalized across the 85–105 km region. Median uncertainty (bias) with altitude is co-plotted for each profile in a–c (d).

the dynamic instability threshold likelihood exceeded the convective instability threshold likelihood by 5% on average. Above 92 km, this difference increased to 11%. This trend mirrors that published by Li et al. (2005a), who found that overturning structures associated with instabilities are most commonly found between 96–100 km in the MLT region. Furthermore, Li et al. found that the dynamical instability threshold likelihood is greater above 93 km than below, which was similarly observed in this study. However, whereas Li et al. found a nearly constant likelihood of $Ri < 0$ across the mesopause region, Fig. 3d shows a sharp increase in convective instability threshold likelihood above 93 km. The convection instabilities are prevalent on the top side of MILs where the temperature gradient becomes superadiabatic (Li et al., 2005a).

Measurement uncertainties for N^2, wind shear, and Ri profiles are respectively shown in Fig. 4a–c. Uncertainties were estimated at 500 m, 160 s resolution from reconstructed temperature and wind profiles and

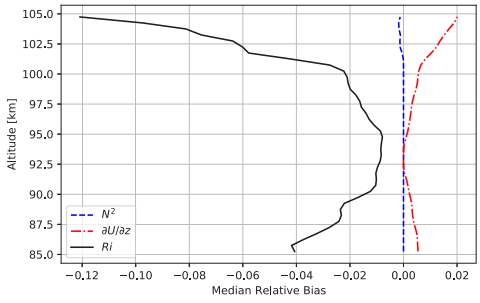

Fig. 5. Median relative measurement bias with altitude for N^2, wind shear, and Ri. Biases were estimated via Monte Carlo simulation.

uncertainties via Eqs. (22)–(24)

$$\sigma_{N_i^2} \approx \frac{g}{\mu_{T_i}\Delta z}\sqrt{\sigma_{T_{i+1}}^2 + \sigma_{T_i}^2\left[1+\left(\frac{\Delta z}{g}\mu_{N_i^2}\right)^2\right]} \tag{22}$$

$$\sigma_{\partial U_i/\partial z} \approx \frac{\sqrt{(\sigma_{u_{i+1}}^2+\sigma_{u_i}^2)(\mu_{u_{i+1}}-\mu_{u_i})^2+(\sigma_{v_{i+1}}^2+\sigma_{v_i}^2)(\mu_{v_{i+1}}-\mu_{v_i})^2}}{\Delta z^2\mu_{\partial U_i/\partial z}} \tag{23}$$

$$\sigma_{Ri_i} \approx \left|\mu_{Ri_i}\right|\sqrt{\left(\frac{\sigma_{N_i^2}}{\mu_{N_i^2}}\right)^2+\left(\frac{\sigma_{(\partial U_i/\partial z)^2}}{\mu_{(\partial U_i/\partial z)^2}}\right)^2} \tag{24}$$

for N^2, wind shear, and Ri respectively, with square wind shear uncertainty given by Eq. (25).

$$\sigma_{(\partial U_i/\partial z)^2} \approx \frac{\sqrt{(\sigma_{u_{i+1}}^2+\sigma_{u_i}^2)(\mu_{u_{i+1}}-\mu_{u_i})^2+(\sigma_{v_{i+1}}^2+\sigma_{v_i}^2)(\mu_{v_{i+1}}-\mu_{v_i})^2}}{\Delta z^2/2} \tag{25}$$

In Eqs. (22)–(25), σ_ζ denotes the calculated one-sigma measurement uncertainty of parameter ζ, μ_ζ is a measurement of parameter ζ, and subscripts i and $i+1$ denote vertically adjacent observations of the given parameter, with $\Delta z = z_{i+1} - z_i$. Derivations of Eqs. (22)–(25) are included in Appendix.

Temperature and wind measurements are corrected for biases arising primarily from Na absorption cross-section uncertainty and laser frequency shifts, respectively, through correction for the Hanle effect (Papen et al., 1995) and application of a zero-mean vertical wind constraint in the 80–115 km region. Wind and temperature error distributions used to determine error bias and uncertainty were chosen to be uncorrelated (Papen et al., 1995) and zero-mean Gaussian, with max measurement uncertainties corresponding to the $\pm 3\sigma$ points of the distributions. Measurement bias in N^2, wind shear, and Ri profiles was assessed via Monte Carlo simulation. For each wind and temperature measurement at 500 m, 160 s resolution, 10^4 calculations of Eqs. (3)–(5) were performed over random realizations of wind and temperature, with samples drawn from the corresponding error distributions. Output error distributions were estimated from histograms of each set of realizations. Bias was estimated as the difference between the reported measurements and the mode of each simulated output distribution. Fig. 4d shows the estimated Ri bias distribution with altitude.

Median relative bias with altitude is plotted in Fig. 5 for N^2, wind shear, and Ri measurements. Relative bias was calculated at 500 m, 160 s resolution from the ratio between bias estimates and parameter measurements. Wind shear and Ri profiles exhibited positive and negative relative biases on the order of 2% magnitude and 1%–10% magnitude, respectively, across the 85–105 km region. Reported Ri and wind shear measurements in Fig. 3 were corrected for measurement bias. After bias correction, measurements with relative and absolute uncertainties respectively in excess of 20% and 2×10^{-4} s^{-2} for N^2, 40% and 20 $ms^{-1}km^{-1}$ for wind shear, and 40% and 0.05 for Ri were omitted from the mean profiles presented in Fig. 3. In Eqs. (22)–(25), measurements were corrected for bias prior to uncertainty estimation. N^2 measurements did not exhibit significant bias.

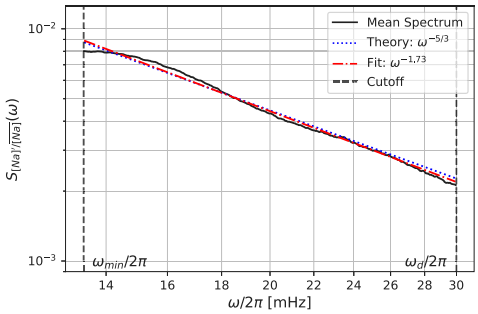

Fig. 6. Mean temporal spectrum over 25 nights of data acquired at ALO. The mean profile was calculated from independent altitude profiles binned to 25 m, 12 s resolution. Vertical dashed lines denote the lower and upper cutoffs for the turbulence subrange (13 mHz and 30 mHz, respectively). The theoretical $\omega^{-5/3}$ relation (dotted) and a power law (ω^{-b}) least-squares fit to the mean observed spectrum (dash–dot) are co-plotted, where $b = -1.73$.

6. Eddy diffusion measurements from Na fluctuations

The mean temporal Na density fluctuation spectrum across the 85–105 km region is shown in Fig. 6 for the turbulence subrange, along with the corresponding least-squares power law fit. The fit of $\omega^{-1.73}$ agrees well with the expected theoretical result ($\omega^{-5/3}$). Total spectral power in the turbulence subrange is calculated from the summation of the power law fit between the plotted inner and outer scales. Cutoffs of 13 mHz and 30 mHz were chosen, with the former corresponding to the continuous zenith observation period (78 s) and the latter to the maximum frequency before which additive white noise began to dominate and flatten the observed spectrum.

Average turbulence-induced Na layer perturbations in the 85–105 km region are shown in Fig. 7a. The Na layer perturbation profile closely mirrors the Gaussian average density profile, which is a manifestation of the relation between Na scale height and layer sensitivity to turbulence as described by Eq. (12). Layer perturbations decreased from $78\%^2$ (8.9%) at 85 km to a minimum of $21\%^2$ (4.5%) across the 85–105 km region at 92.5 km, then increased to a maximum of $444\%^2$ (21%) at 102.5 km. Above 102.5 km, the mean profile remained approximately flat. Nightly variability in Na layer perturbation amplitude was significant, with a standard deviation between 40% and 130% of the mean profile.

The mean neutral perturbation profile is shown in Fig. 7b. Average layer perturbations ranged from $1.5\%^2$ (1.2%) at 98 km to $40\%^2$ (6.4%) at 105 km. Mean perturbation amplitude generally increased with increasing altitude across the region, with the exception of a decrease between 93 km and 98 km. Measurements with large neutral-to-Na (>10:1) amplitude perturbation ratios, which can occur for $\gamma H_p \approx H_{Na}$, were omitted to avoid the singularity in Eq. (12). Since the singularity is not at a fixed altitude as the Na density profiles varies with time, neutral density fluctuations can be derived at all altitudes when an extended dataset is used. Comparing Fig. 2c and Fig. 3d with Fig. 7b, the decrease in neutral fluctuation amplitude was accompanied by a negative temperature gradient and region of heightened convective and dynamical instability. The observed decrease could potentially be attributed to the reduced mean atmospheric stability in the region.

The variance of relative Na layer perturbations was on average 4–50 times stronger than that of the associated neutral perturbations, corresponding to an amplitude ratio of 2–7. The positive two-sigma amplitude ratio across the dataset analyzed was 11.5. This agrees well with Kelley et al. (2003) and Gardner and Liu (2014), who found that layer perturbation amplitude can be as large as 10–15 times that of the neutral perturbation amplitude. However, average neutral density fluctuations were larger than expected compared to Lübken (1997), who observed neutral fluctuations on the order of 0.1–1.0% in the 85–100 km region.

The nightly mean turbulent eddy diffusion (k_{zz}^{Turb}) profiles determined from neutral density fluctuations are co-plotted in Fig. 8a, with the mean profile over the dataset shown in Fig. 8b–c. Profile uncertainty was less than 10^5 cm^2s^{-1} across the 85–105 km region. Mean k_{zz}^{Turb} decreased from 5.0×10^5 cm^2s^{-1} at 85 km to 2.2×10^5 cm^2s^{-1} at 93 km. Variation in the mean turbulent eddy diffusion profile was strongest between 93 km and 98 km, with the one-sigma nightly variability ranging from 60% to 360% of the mean. Above 98 km altitude, mean k_{zz}^{Turb} increased from 1.4×10^5 cm^2s^{-1} to a maximum of 4.5×10^6 cm^2s^{-1} near 105 km.

In the 93–98 km region, the unsmoothed profile (Fig. 8b) exhibited several sharp peaks and troughs spaced roughly 1 km apart. This effect correlates well to the increased instability likelihood seen in Fig. 3d, which was enhanced over the same altitude region compared to the mean across the 85–105 km region. Each peak in the mean profile can be attributed to contributions from one or two nights of observations, as seen in Fig. 8a, with the majority of nights remaining closer to the mean. This result, in addition to the large variance of the mean profile, reinforces that turbulence is a sporadic and highly variable process in the MLT region, and that when aiming to characterize mean properties of turbulence, either additional treatment should be applied to outlier profiles or a sufficiently large dataset should be used, irrespective of S/N concerns.

The relationship between neutral perturbation amplitude and k_{zz}^{Turb} across the 85–105 km region agrees well with Lübken (1997) – when taking scaling due to incomplete observation (~38%) of the turbulence spectrum into account — who measured a turbulent eddy diffusion coefficient of 8×10^5 cm^2s^{-1} for neutral density fluctuations on the order of 1%. In comparison, unscaled average neutral fluctuations and k_{zz}^{Turb} across the 85–105 km region were 2.2% and 7.6×10^5 cm^2s^{-1}, respectively, for the current study. The measured mean k_{zz}^{Turb} also compares favorably with Liu (2009), who measured annual mean k_H (and therefore k_{zz}) at Starfire Optical Range, NM (SOR) ranging from 1×10^6 cm^2s^{-1} to 4×10^6 cm^2s^{-1} across the 85–100 km region, with minimum mean total eddy diffusion observed near the equinoctial periods.

7. Comparison of turbulent eddy diffusion coefficient measurements

Na density method measurements of k_{zz}^{Turb} were first compared against Doppler method measurements of heat flux over the 25-night ALO dataset, with eddy diffusion and heat flux related by Eq. (11). The background parameters shown in Figs. 2–3 were used in the calculation of the relation. Heat flux observations were binned to 500 m resolution, smoothed with a 2.5 km Hamming window, and interpolated to 250 m resolution for purpose of comparison. Additional detail on the Doppler method is provided in Guo et al. (2017). As in the case of Na density method measurements, observations of heat flux via the Doppler method were limited to 78 s intervals, such that observation of heat flux over the full turbulence subrange was not possible.

Doppler method measurements of k_{zz}^{Turb} and heat flux are respectively shown in Fig. 9a and Fig. 9b, where the former is determined from Eq. (11). Na density method results are also co-plotted, with heat flux measurements similarly related to k_{zz}^{Turb} observations. Overall, the Doppler and Na method yielded similar profiles. Heat flux profiles ranged between -0.05 Kms^{-1} and -0.6 Kms^{-1} in the 85–100 km region. Profile magnitude was on average largest between 93 km and 98 km altitude, again exhibiting behavior consistent with expectations given the reduced mean stability in the region. While the Doppler method heat flux measurements were larger in magnitude than those of the Na density method, the Na density profile variability aligned well with the increase in heat flux observed by the Doppler method.

Na density method results were next compared against mean k_{zz}^{Turb} in the 85–100 km region as determined from 150 hours of vertical-only

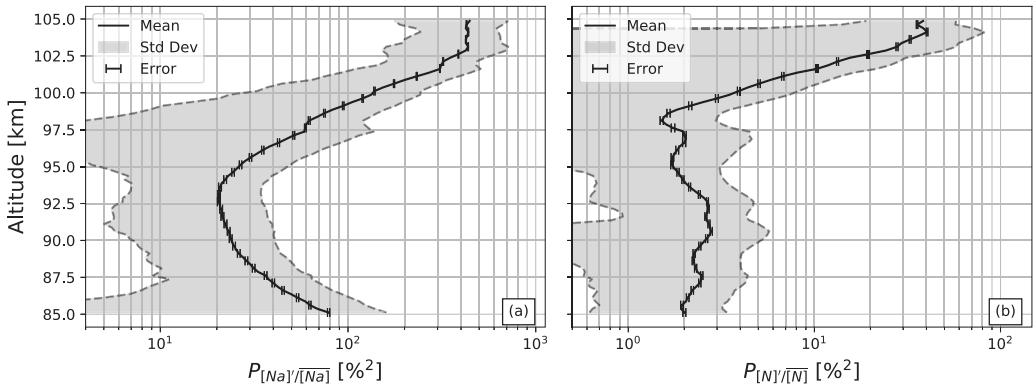

Fig. 7. Turbulence-induced layer perturbations at 250 m resolution. Mean profiles are denoted by solid lines, while one-sigma variability over the dataset analyzed is bounded by dashed lines. (a) Average Na turbulence fluctuation profile over 25 nights of ALO data. (b) Mean neutral density turbulence fluctuation profile between 85 km and 105 km altitude.

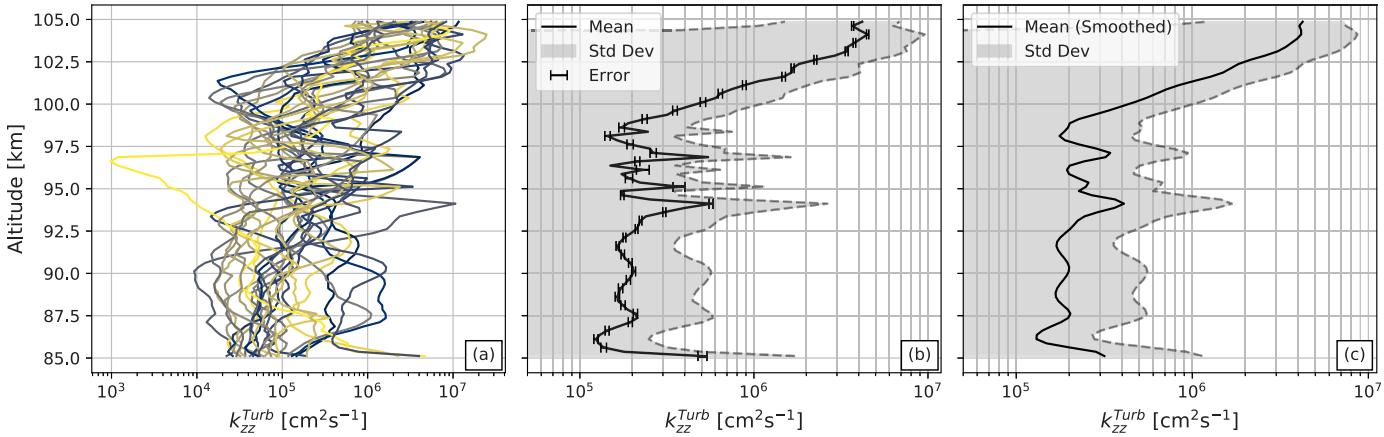

Fig. 8. (a) Superposition of nightly mean k_{zz}^{Turb} profiles as determined from 25 nights of observational data over ALO. Variability in the nightly mean profiles was considerable (60%–360% of the mean profile); however, error in the mean profile was less than 10^5 cm^{2}s^{-1} at all analyzed altitudes. (b) Mean k_{zz}^{Turb}. One-sigma variability over the dataset analyzed is shaded and bounded by dashed lines. Observed k_{zz}^{Turb} decreased from 5.0×10^5 cm^{2}s^{-1} at 85 km to 2.2×10^5 cm^{2}s^{-1} at 93 km. Several layers of alternating enhanced and depleted eddy transport were present between 93 km and 98 km, with the mean profile in the region ranging from 1.2×10^5 cm^{2}s^{-1} to 5.7×10^5 cm^{2}s^{-1}. Above 98 km, a large increase in the mean profile was observed, reaching 4.5×10^6 cm^{2}s^{-1} near 105 km. (c) Same as (b), but smoothed with a 1.5 km Hamming window.

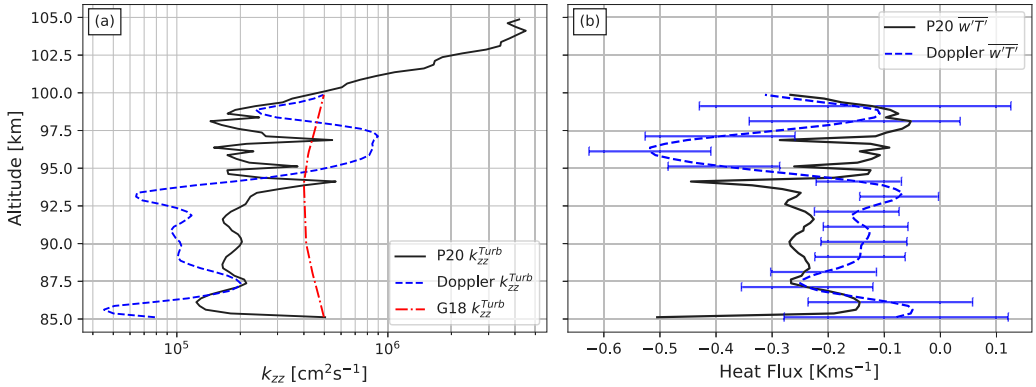

Fig. 9. (a) Comparison of k_{zz}^{Turb} determined from Na density method (P20, solid) and Doppler method measurements over the same dataset (dashed) and k_{zz}^{Turb} as determined from 150 hours of vertical-only ALO measurements in the 85–100 km region (G18, dash–dot). Na density and Doppler method measurements were obtained over 25 nights of ALO data for timescales smaller than 78 s, while the vertical-only profile included contributions across the full turbulence subrange (up to N). Na density and Doppler profiles for the 25-night dataset exhibited similar mean behavior and variability in the 85–100 km region. (b) Comparison of heat flux as measured from the Na density (P20, solid) and Doppler (dashed) methods in the 85–100 km region. Mean heat flux ranged between −0.05 Kms^{-1} and −0.6 Kms^{-1}.

Doppler method measurements over ALO (Gardner, 2018). Vertical-only measurements enabled observation of the full turbulence subrange, including perturbations between $N/2\pi$ (~3 mHz) and 13 mHz that were not observable in the 25-night dataset due to integration period limitations. Shown in Fig. 9a, the vertical-only mean profile varied between 4×10^5 cm^{2}s^{-1} and 5×10^5 cm^{2}s^{-1}, with a minimum at 94 km and maxima at 85 km and 100 km. Na density and Doppler method measurements over the 25-night ALO dataset are expected to have characterized 38% of the total turbulence spectral power. The reported k_{zz}^{Turb} for the Na density and Doppler methods are therefore

expected to be a factor of 2.65 smaller than the total k_{zz}^{Turb} reported by Gardner (2018).

It is noted in Fig. 8 that the largest k_{zz} values are above 100 km, exceeding 10^6 cm^{2}s^{-1} above 101 km. Prior investigation above 100 km includes the more than 400 chemical release soundings summarized by Larsen (2002), where average wind shears were large, with an average altitude of 105 km. The analysis by Qian et al. (2009) deduced from thermosphere measurements showed that k_{zz} averaged $>10^6$ cm^{2}s^{-1} above 97 km. Global measurements of O from O(^{1}S) (green line) by SCIAMACHY satellite resulted in a global mean k_{zz} of 1.1×10^6 cm^{2}s^{-1} above 100 km (Swenson et al., 2019). The inference that the results herein (Fig. 8) from turbulence only are comparable to global mean k_{zz}, and that large shears are statistically ever-present over a large range of latitudes, suggests that KHIs or breaking gravity waves (and turbulence) may play a larger, or even dominant role at this mountain site, in vertical transport than the relatively minor role played at lower altitudes (Gardner, 2018; Fritts et al., 2018). Though the vertical-only results generally agree with this hypothesis, direct comparison over the full turbulence subrange is required to rigorously verify such a link.

8. Conclusion

In summary, this study has (1) detailed the "Na density" method, which enables observation of turbulence to higher altitudes than the Doppler ($\overline{w'T'}$) method for a common measurement system, and (2) examined 25 nights of Na resonance-fluorescence lidar measurements of temperature, vertical and horizontal wind, Na density, atmospheric stability (Ri), and turbulent eddy diffusion (k_{zz}^{Turb}) at timescales shorter than 78 s in the 85–105 km region over the Andes Lidar Observatory (30.3°S, 70.7°W). Na density method measurements were compared with Doppler method measurements from the same dataset in the 85–100 km region, as well as Doppler method measurements of k_{zz}^{Turb} spanning the full turbulence subrange, as described in Gardner (2018).

Based on the stability measurements in Fig. 3d, k_{zz}^{Turb} measurements in Fig. 8, and measurement comparison in Fig. 9, it is reasonable to conclude the following:

1. The Na density method is sensitive to turbulence in the 85–105 km region.
2. When applied to the same set of observations with sufficient S/N, the Na density and Doppler methods yield comparable results.
3. The Na density method is suitable for monthly, seasonal, and annual trends in the 85–105 km region at 25 m, 12 s resolution for an 0.9 Wm^2 power–aperture product system, corresponding to a minimum total observation time of approximately 100 minutes.
4. For the dataset analyzed, the mean turbulent eddy diffusion coefficient (k_{zz}^{Turb}) ranged between 1.2×10^5 cm^{2}s^{-1} and 4.5×10^6 cm^{2}s^{-1} in the 85–105 km region over ALO for continuous observation periods shorter than 78 s.
5. Turbulence-induced eddy diffusion varies considerably between observation periods at a given altitude (standard deviation of ±60%–360% of the mean over the observed dataset).
6. Increased instability likelihood in the 93–98 km region corresponded to increased turbulent eddy diffusion over the same region for the dataset analyzed.
7. Mean observed turbulent eddy diffusion increased sharply – by over an order of magnitude – from 100 km to 105 km altitude, implying that eddy diffusion plays a strong role in atmospheric dynamics near the turbopause.
8. The fact that k_{zz}^{Turb} (Fig. 9) suggests that either (or both) KHIs or gravity waves play a larger role in vertical transport above 95 km than below at this mountain site, where below, dissipating wave effects dominate (Gardner, 2018).

Further investigation of winds and shears are being measured with recently added meteor radar capability at the ALO site. Future studies should employ continuous zenith observation for characterization of turbulence up to the Brunt–Väisälä frequency, though with the caveat that horizontal (and therefore Ri) measurements cannot be made over the same time period when collecting observations with a comparable measurement system.

Acknowledgments

Support for C. Philbrick, G. Swenson, and F. Vargas was provided by the National Science Foundation, USA AGS12-42895 and NSF AGS 11-10334 grants. A. Liu and F. Yang were supported by National Science Foundation grant AGS-1115249. The authors would like to thank two anonymous reviewers for their feedback and recommendations.

Appendix. Ri Measurement uncertainty

Given a set of temperature and horizontal wind measurements and their associated uncertainties, we would like to estimate Ri measurement uncertainty through propagation of error. The approach presently taken assumes that measurement errors are uncorrelated and can be described by a Gaussian distribution with $\pm3\sigma$ bounds defining total measurement uncertainty.

First, let us consider the uncertainty distribution of N^2. We would like to find the standard deviation of the uncertainty distribution, σ_{N^2}. Starting from Eq. (3), we have

$$N_i^2 \approx \frac{g}{T_i}\left(\frac{T_{i+1}-T_i}{\Delta z}+\Gamma_{ad}\right)=\frac{1}{T_i}\left[\frac{g}{\Delta z}(T_{i+1}-T_i)+g\Gamma_{ad}\right]=\frac{f_{\alpha_i}}{T_i} \tag{26}$$

for vertically adjacent temperature measurements T_i and T_{i+1}, $z_{i+1}-z_i=\Delta z$, and $i\in[0,M-2]$ for M altitude bins. For a measurement uncertainty $\pm3\sigma_{T_i}$ of temperature μ_{T_i}, let $T_i\sim G(\mu_{T_i},\sigma_{T_i}^2)$, with all T_i mutually uncorrelated. Note that the notation $G(\mu,\sigma^2)$ is used to denote the normal distribution. Then, f_{α_i} is distributed as

$$f_{\alpha_i}\sim G\left(\frac{g}{\Delta z}(\mu_{T_{i+1}}-\mu_{T_i})+g\Gamma_{ad},\frac{g^2}{\Delta z^2}(\sigma_{T_{i+1}}^2+\sigma_{T_i}^2)\right) \tag{27}$$

The standard deviation, σ_Z, of the distribution $Z=X/Y$ resulting from the ratio of two uncorrelated Gaussian random variables, X and Y, is approximately given by Díaz-Francés and Rubio (2013)

$$\sigma_Z\approx|\mu_Z|\sqrt{\left(\frac{\sigma_X}{\mu_X}\right)^2+\left(\frac{\sigma_Y}{\mu_Y}\right)^2} \tag{28}$$

Therefore, for $N_i^2=f_{\alpha_i}/T_i$, we have

$$\sigma_{N_i^2}\approx\left|\mu_{N_i^2}\right|\sqrt{\left(\frac{\sigma_{f_{\alpha_i}}}{\mu_{f_{\alpha_i}}}\right)^2+\left(\frac{\sigma_{T_i}}{\mu_{T_i}}\right)^2} \tag{29}$$

where $\mu_{N_i^2}$ is given by

$$\mu_{N_i^2}=\frac{g}{\mu_{T_i}}\left(\frac{\mu_{T_{i+1}}-\mu_{T_i}}{\Delta z}+\Gamma_{ad}\right) \tag{30}$$

This simplifies to the result

$$\sigma_{N_i^2}\approx\frac{g}{\mu_{T_i}\Delta z}\sqrt{\sigma_{T_{i+1}}^2+\sigma_{T_i}^2\left[1+\left(\frac{\Delta z}{g}\mu_{N_i^2}\right)^2\right]} \tag{31}$$

Next, we would like to find the standard deviation of the wind shear error distribution, $\sigma_{\partial U_i/\partial z}$. Eq. (5) may be approximated as

$$\frac{\partial U_i}{\partial z}\approx\frac{1}{\Delta z}\sqrt{(u_{i+1}-u_i)^2+(v_{i+1}-v_i)^2} \tag{32}$$

where u_i and v_i respectively denote zonal and meridional wind measurements at altitude z_i. Note that for $Z=\sqrt{aX^2+bY^2}$, where X and

Y are uncorrelated Gaussian random variables, a and b are scalars, and Z is approximated as Gaussian, σ_Z is given by

$$\sigma_Z^2 \approx a^2 \left(\frac{\mu_X \sigma_X}{\mu_Z} \right)^2 + b^2 \left(\frac{\mu_Y \sigma_Y}{\mu_Z} \right)^2 \tag{33}$$

For $u_i \sim G(\mu_{u_i}, \sigma_{u_i}^2)$ and $v_i \sim G(\mu_{v_i}, \sigma_{v_i}^2)$, we accordingly have

$$\sigma_{\partial U_i/\partial z} \approx \frac{\sqrt{(\sigma_{u_{i+1}}^2 + \sigma_{u_i}^2)(\mu_{u_{i+1}} - \mu_{u_i})^2 + (\sigma_{v_{i+1}}^2 + \sigma_{v_i}^2)(\mu_{v_{i+1}} - \mu_{v_i})^2}}{\Delta z^2 \mu_{\partial U_i/\partial z}} \tag{34}$$

with all zonal and meridional wind measurement errors mutually uncorrelated. Square wind shear uncertainty is obtained as

$$\sigma_{(\partial U_i/\partial z)^2} \approx \frac{\sqrt{(\sigma_{u_{i+1}}^2 + \sigma_{u_i}^2)(\mu_{u_{i+1}} - \mu_{u_i})^2 + (\sigma_{v_{i+1}}^2 + \sigma_{v_i}^2)(\mu_{v_{i+1}} - \mu_{v_i})^2}}{\Delta z^2/2} \tag{35}$$

where the relation $\sigma_Z \approx 2\mu_X \sigma_X$ has been used for $Z = aX^2$, with $X \sim G(\mu_X, \sigma_X^2)$ and Z approximated as Gaussian.

Lastly, the standard deviation of the Ri error distribution, σ_{Ri_i}, is obtained as

$$\sigma_{Ri_i} \approx \left| \mu_{Ri_i} \right| \sqrt{\left(\frac{\sigma_{N_i^2}}{\mu_{N_i^2}} \right)^2 + \left(\frac{\sigma_{(\partial U_i/\partial z)^2}}{\mu_{(\partial U_i/\partial z)^2}} \right)^2} \tag{36}$$

from Eqs. (4) and (28).

References

Allen, M., Lunine, J.I., Yung, Y.L., 1984. The vertical distribution of ozone in the mesosphere and lower thermosphere. J. Geophys. Res. 89 (D3), 4841–4872.

Allen, M., Yung, Y.L., Waters, J.W., 1981. Vertical transport and photochemistry in the terrestrial mesosphere and lower thermosphere (50–120 km). J. Geophys. Res. 86 (A5), 3617–3627.

Banks, P.M., Kockarts, G., 1973. Aeronomy. Academic Press, New York.

Bills, R.E., Gardner, C.S., Franke, S.F., 1991. Na Doppler/temperature lidar: initial mesopause region observations and comparison with the Urbana MF radar. J. Geophys. Res. 96, 22701–22707.

Bishop, R.L., Larsen, M.F., Hecht, J.H., Liu, A.Z., Gardner, C.S., 2004. TOMEX: Mesospheric and lower thermospheric diffusivities and instability layers. J. Geophys. Res. 109, D02S03.

Chu, X., Papen, G.C., 2005. Resonance Fluorescence Lidar for Measurements of the Middle and Upper Atmosphere, in Laser Remote Sensing. In: Opt. Sci. Eng., CRC Press, Boca Raton, FL, pp. 179–432.

Colegrove, F.D., Hanson, W.B., Johnson, F.S., 1965. Eddy diffusion and oxygen transport in the lower thermosphere. J. Geophys. Res. 70 (19), 4931–4941.

Colegrove, F.D., Johnson, F.S., Hanson, W.B., 1966. Atmospheric composition in the lower thermosphere. J. Geophys. Res. 71 (9), 2227–2236.

Das, U., Sinha, H.S.S., Sharma, S., Chandra, H., Das, S.K., 2009. Fine structure of the low-latitude mesospheric turbulence. J. Geophys. Res. 114, D10111.

Díaz-Francés, E., Rubio, F.J., 2013. On the existence of a normal approximation to the distribution of the ratio of two independent normal random variables. Stat. Pap. 54, 309–323.

Fritts, D.C., Alexander, M.J., 2003. Gravity wave dynamics and effects in the middle atmosphere. Rev. Geophys. 41 (1), 1003.

Fritts, D.C., Vanzandt, T.E., 1993. Spectral estimates of gravity wave energy and momentum fluxes Part I: Energy dissipation, acceleration, and constraints. J. Atmos. Sci. 50, 3685–3694.

Fritts, D.C., Wang, L., Baumgarten, G., Miller, A.D., Geller, M.A., Jones, G., Vinokurov, J., 2017. High-resolution observations and modeling of turbulence sources, structures, and intensities in the upper mesosphere. J. Atmos. Sol.-Terr. Phys. 162, 57–78.

Fritts, D.C., Wang, L., Laughman, B., Lund, T.S., Collins, R.L., 2018. Gravity wave dynamics in a mesospheric inversion layer: 2. Instabilities, turbulence, fluxes, and mixing. J. Geophys. Res. Atmos. 123, 649–670.

Gardner, C.S., 1996. Testing theories of atmospheric gravity wave saturation and dissipation. J. Atmos. Terr. Phys. 58 (13), 1575–1589.

Gardner, C.S., 1998. Theoretical models for gravity wave horizontal wave number spectra: Effects of wave field anisotropies. J. Geophys. Res. 103 (D6), 6417–6425.

Gardner, C.S., 2018. Role of wave-induced diffusion and energy flux in the vertical transport of atmospheric constituents in the mesopause region. J. Geophys. Res. 123, 6581–6604.

Gardner, C.S., Liu, A.Z., 2010. Wave-induced transport of atmospheric constituents and its effect on the mesospheric Na layer. J. Geophys. Res. 115, D20302.

Gardner, C.S., Liu, A.Z., 2014. Measuring eddy heat, constituent, and momentum fluxes with high-resolution Na and Fe Doppler lidars. J. Geophys. Res. Atmos. 119, 10583–10603.

Gardner, C.S., Liu, A.Z., Guo, Y., 2017. Vertical and horizontal transport of mesospheric Na: implications for the mass influx of cosmic dust. J. Atmos. Sol. -Terr. Phys. 162, 192–202.

Gardner, C.S., Vargas, F.A., 2014. Optimizing three-frequency Na, Fe, and He lidars for measurements of wind, temperature, and species density and the vertical fluxes of heat and constituents. Appl. Opt. 53, 4100–4116.

Gardner, C.S., Yang, W., 1998. Measurements of the dynamical cooling rate associated with the vertical transport of heat by dissipating gravity waves in the mesopause region at the Starfire Optical Range, New Mexico. J. Geophys. Res. 103 (D14), 16909–16926.

Gossard, E.E., Hooke, W.H., 1975. Waves in the Atmosphere, Atmospheric Infrasound and Gravity Waves – Their Generation and Propagation. Elsevier Sci., New York.

Guo, Y., Liu, A.Z., Gardner, C.S., 2017. First Na lidar measurements of turbulence heat flux, thermal diffusivity, and energy dissipation rate in the mesopause region. Geophys. Res. Lett. 44, 5782–5790.

Hakamata, T., 2007. Photomultiplier Tubes: Basics and Applications, third ed. Hamamatsu Photonics K. K., Japan.

Hayya, J., Armstrong, D., Gressis, N., 1975. A note on the ratio of two normally distributed variables. Manag. Sci. 21 (11), 1338–1341.

Hecht, J.H., 2004. Instability layers and airglow imaging. Rev. Geophys. 42, RG1001.

Heisenberg, W., 1948. On the theory of statistical and isotropic turbulence. Proc. Royal Soc. A 195 (1042), 402–406.

Hickey, M.P., Plane, J.M.C., 1995. A chemical-dynamical model of wave-driven sodium fluctuations. Geophy. Res. Lett. 22 (20), 2861–2864.

Hines, C.O., 1960. Internal atmospheric gravity waves at ionospheric heights. Can. J. Phys. 38, 1441–1481.

Hines, C.O., 1971. Generalization of the richardson criterion for the onset of atmospheric turbulence. Q. J. R. Meteorol. Soc. 97, 429–439.

Hodges, R.R., 1967. Generation of turbulence in the upper atmosphere by internal gravity waves. J. Geophys. Res. 72 (13), 3455–3458.

Hodges, R.R., 1969. Eddy diffusion coefficients due to instabilities in internal gravity waves. J. Geophys. Res. 74 (16), 4087–4090.

Huang, T.-Y., Hickey, M.P., Tuan, T.-F., Dewan, E.M., Picard, R.H., 2002. Further investigations of a mesospheric inversion layer observed in the ALOHA-93 campaign. J. Geophys. Res. 107 (D19), 4408.

Huang, T.-Y., Hur, H., Tuan, T.F., Li, X., 1998. Sudden narrow temperature-inversion-layer formation in ALOHA-93 as a critical-layer-interaction phenomenon. J. Geophys. Res. 103 (D6), 6323–6332.

Kelley, M.C., Kruschwitz, C.A., Gardner, C.S., Drummond, J.D., Kane, T.J., 2003. Mesospheric turbulence measurements from persistent Leonid meteor train observations. J. Geophys. Res. 108 (D8), 8454.

Kolmogorov, A., 1941. Dissipation of energy in the locally isotropic turbulence. Dokl. Akad. Nauk SSSR 32, 16–18.

Krueger, D.A., She, C.-Y., Yuan, T., 2015. Retrieving mesopause temperature and line-of-sight wind from full-diurnal-cycle Na lidar observations. Appl. Opt. 54 (32), 9469–9489.

Larsen, M.F., 2002. Winds and shears in the mesosphere and lower thermosphere: Results from four decades of chemical release wind measurements. J. Geophys. Res. 107 (A8), 1215.

Li, F., Liu, A.Z., Swenson, G.R., 2005a. Characteristics of instabilities in the mesopause region over Maui, Hawaii. J. Geophys. Res. 110, D09S12.

Li, T., She, C.-Y., Liu, H.-L., Yue, J., Nakamura, T., Krueger, D.A., Wu, Q., Dou, X., Wang, S., 2009. Observation of local tidal variability and instability, along with dissipation of diurnal tidal harmonics in the mesopause region over Fort Collins, Colorado (41°N, 105°W). J. Geophys. Res. 114, D06106.

Li, F., Swenson, G.R., Hecht, J.H., Robinson, W.A., 2005b. Observations of gravity wave breakdown into ripples associated with dynamical instabilities. J. Geophys. Res. 110, D09S11.

Lindzen, R.S., 1981. Turbulence and stress owing to gravity wave and tidal breakdown. J. Geophys. Res. 86, 9707–9714.

Liu, A.Z., 2009. Estimate eddy diffusion coefficients from gravity wave vertical momentum and heat fluxes. Geophys. Res. Lett. 36, L08806.

Liu, A.Z., Guo, Y., 2016. Photomultiplier tube calibration based on Na lidar observation and its effect on heat flux bias. Appl. Opt. 55, 9467–9475.

Liu, A.Z., Guo, Y., Vargas, F., Swenson, G.R., 2016. First measurement of horizontal wind and temperature in the lower thermosphere (105–140 km) with a Na Lidar at Andes Lidar Observatory. Geophys. Res. Lett. 43, 2374–2380.

Liu, H.L., Hagan, M.E., 1998. Local heating/cooling of the mesosphere due to gravity wave and tidal coupling. Geophys. Res. Lett. 25 (15), 2941–2944.

Lübken, F.J., 1997. Seasonal variation of turbulent energy dissipation rates at high latitudes as determined by in situ measurements of neutral density fluctuations. J. Geophys. Res. 102 (D12), 13441–13456.

Marsh, D.R., Garcia, R.R., 2007. Attribution of decadal variability in lower-stratospheric tropical ozone. Geophys. Res. Lett. 34, L21807.

Marsh, D.R., Janches, D., Feng, W., Plane, J.M.C., 2013. A global model of meteoric sodium. J. Geophys. Res. Atmos. 118, 11442–11452.

Meriwether, J.W., Dao, P.D., McNutt, R.T., Klemetti, W., Moskowitz, W., Davidson, G., 1994. Rayleigh lidar observations of mesosphere temperature structure. J. Geophys. Res. 99 (D8), 16973–16987.

Meriwether, J.W., Gardner, C.S., 2000. A review of the mesosphere inversion layer phenomenon. J. Geophys. Res. 105 (D10), 12405–12416.
Miles, J.W., Howard, L.N., 1964. Note on a heterogeneous shear flow. J. Fluid Mech. 20 (2), 331–336.
Nappo, C., 2012. An Introduction to Atmospheric Gravity Waves, Vol. 102, second ed. Academic Press, Cambridge, MA, p. 400.
Palmer, T.L., Fritts, D.C., Andreassen, Ø., 1996. Evolution and breakdown of Kelvin–Helmholtz billows in stratified compressible flows. Part II: Instability structure, evolution, and energetics. J. Geophys. Res. 53 (22), 3192–3212.
Papen, G.C., Pfenninger, W.M., Simonich, D.M., 1995. Sensitivity analysis of Na narrowband wind-temperature lidar systems. Appl. Opt. 34 (3), 480–498.
Plane, J.M.C., 1991. The chemistry of meteoric metals in the Earth's upper atmosphere. Int. Rev. Phys. Chem. 10 (1), 55–106.
Qian, J., Gu, Y., Gardner, C.S., 1998. Characteristics of the sporadic Na layers observed during the Airborne Lidar and Observations of Hawaiian Airglow/Airborne Noctilucent Cloud (ALOHA/ANLC-93) campaigns. J. Geophys. Res. 103 (D6), 6333–6347.
Qian, L., Solomon, S.C., Kane, T.J., 2009. Seasonal variation of thermospheric density and composition. J. Geophys. Res. 114, A01312.
Rees, D., Roper, R.G., Lloyd, K.H., Low, C.H., 1972. Determination of the structure of the atmosphere between 90 and 250 km by means of contaminant releases at Woomera, May 1968. Philos. Trans. R. Soc. Lond. Ser. A 271, 631–663.
Richardson, L.F., 1920. The supply of energy from and to atmospheric eddies. Proc. Royal Soc. A 97, 354–373.
Sato, T., Tsuda, T., Kato, S., Morimoto, S., Fukao, S., Kimura, I., 1985. High-resolution MST observations of turbulence by using the MU radar. Radio Sci. 20 (6), 1452–1460.
Schmidlin, F.J., Lee, H.S., Michel, W., 1991. The inflatable sphere: A technique for the accurate measurement of middle atmosphere temperatures. J. Geophys. Res. 96 (D12), 22673–22682.
She, C.Y., Yu, J.R., Chen, H., 1993. Observed thermal structure of a midlatitude mesopause. Geophys. Res. Lett. 20 (7), 567–570.
Shimazaki, T., 1971. Effective eddy diffusion coefficient and atmospheric composition in the lower thermosphere. J. Atmos. Terr. Phys. 33, 1383–1401.
Shimazaki, T., Whitten, R.C., 1976. A comparison of one-dimensional theoretical models of stratospheric minor constituents. Rev. Geophys. 14 (1), 1–12.
Shuai, J., Zhang, S., Huang, C., Yi, F., Huang, K., Gan, Q., Gong, Y., 2014. Climatology of global gravity wave activity and dissipation revealed by SABER/TIMED temperature observations. Sci. China Technol. Sci. 57 (5), 998–1009.
Swenson, G.R., Salinas, C.C.J.H., Vargas, F., Zhu, Y., Kaufmann, M., Jones, Jr., M., Drob, D.P., Liu, A., Yue, J., Yee, J.H., 2019. Determination of global mean eddy diffusive transport in the mesosphere and lower thermosphere from atomic oxygen and carbon dioxide climatologies. J. Geophys. Res. 124, 13519–13533.
Swenson, G.R., Yee, Y., Vargas, F., Liu, A.Z., 2018. Vertical diffusion transport of atomic oxygen in the mesopause region consistent with chemical losses and continuity: Global mean and inter-annual variability. J. Atmos. Sol. -Terr. Phys. 178, 47–57.
Taylor, G.I., 1935. Statistical theory of turbulence. Proc. Royal Soc. A 151 (873), 421–444.
Thrane, E.V., Grandal, B., 1981. Observations of fine scale structure in the mesosphere and lower thermosphere. J. Atmos. Terr. Phys. 43 (3), 179–189.
Weinstock, J., 1978. Vertical turbulent diffusion in a stably stratified fluid. J. Atmos. Sci. 35, 1022–1027.
Weinstock, J., 1981. Energy dissipation rates of turbulence in the stable free atmosphere. J. Atmos. Sci. 38, 880–883.
Widdel, H.U., 1985. Foil clouds as a tool for measuring wind structure and irregularities in the lower thermosphere (92–50 km). Radio Sci. 20 (4), 803–812.
Yue, J., She, C.-Y., Liu, H.-L., 2010. Large wind shears and stabilities in the mesopause region observed by Na wind-temperature lidar at midlatitude. J. Geophys. Res. 115, A10307.
Zhao, Y., Liu, A.Z., Gardner, C.S., 2003. Measurements of atmospheric stability in the mesopause region at starfire optical range, NM. J. Atmos. Sol. -Terr. Phys. 65, 219–232.